Spike-induced ordering: Stochastic neural spikes provide immediate adaptability to the sensorimotor system

Shogo Yonekura[a,1] and Yasuo Kuniyoshi[a,1]

[a]Laboratory for Intelligent Systems and Informatics, Department of Mechano-Informatics, Graduate School of Information Science and Technology, The University of Tokyo, Bunkyo-ku, Tokyo 113-8656, Japan

Edited by Terrence J. Sejnowski, Salk Institute for Biological Studies, La Jolla, CA, and approved April 10, 2020 (received for review June 13, 2019)

Most biological neurons exhibit stochastic and spiking action potentials. However, the benefits of stochastic spikes versus continuous signals other than noise tolerance and energy efficiency remain largely unknown. In this study, we provide an insight into the potential roles of stochastic spikes, which may be beneficial for producing on-site adaptability in biological sensorimotor agents. We developed a platform that enables parametric modulation of the stochastic and discontinuous output of a stochastically spiking neural network (sSNN) to the rate-coded smooth output. This platform was applied to a complex musculoskeletal–neural system of a bipedal walker, and we demonstrated how stochastic spikes may help improve on-site adaptability of a bipedal walker to slippery surfaces or perturbation of random external forces. We further applied our sSNN platform to more general and simple sensorimotor agents and demonstrated four basic functions provided by an sSNN: 1) synchronization to a natural frequency, 2) amplification of the resonant motion in a natural frequency, 3) basin enlargement of the behavioral goal state, and 4) rapid complexity reduction and regular motion pattern formation. We propose that the benefits of sSNNs are not limited to musculoskeletal dynamics. Indeed, a wide range of the stability and adaptability of biological systems may arise from stochastic spiking dynamics.

spiking neural network | instantaneous self-organization | bipedal walking | musculoskeletal system | spike-induced ordering

Stochastic spiking neurons fire transient action potentials to generate irregular spike trains. The stochastic spike train of a presynaptic neuron is propagated toward the synaptic terminal and induces irregular and discontinuous time series of the postsynaptic potential (PSP) in a connected neuron or a muscle cell (1). Conventionally, neural spiking is considered to underlie stable and efficient digitalized signal transmission (2). In addition, recent studies have demonstrated that the transient characteristics of stochastic spikes enable the exotic state transition of a neural network, allowing for spike annealing. Such studies have indicated that stochastically spiking neural networks (sSNNs) enable significantly more rapid and efficient optimization than do networks involving rate-based model neurons (3–5). Nevertheless, other merits of irregular/impulsive PSP time series remain largely unclear.

Theoretically, it is well known that noise is beneficial in a nonlinear excitable system that generates all-or-none responses (i.e., neurons or cells): Noise induces ordering of the nonlinear system and aids in the synchronization and formation of spatiotemporal patterns in the excitable media (6–10). The occurrence of noise-induced ordering (11, 12) is not limited to an excitable system and is observed in other systems such as granular particles perturbed by vibration (12). Thus, it is highly feasible that similar noise-induced ordering effects occur in a dynamical system exposed to stochastic spikes.

The computational results of the present study suggest that an sSNN may be the core prerequisite for realizing the instant adaptability of a biological sensorimotor system. In the following sections, we first briefly describe the sSNN model, following which we discuss the architecture that enables us to modulate the spikiness of PSPs generated by the sSNN, where we define the term spikiness as a root-mean square of the second derivative of the PSPs to represent the impulsive and irregular dynamics of the PSPs. We demonstrate how stochastic spikes help improve the adaptability of a musculoskeletal bipedal walker; we demonstrate that decreases in the spikiness of PSPs lead to a reduction in the adaptability. To further analyze how stochastic spikes help improve the adaptability of a bipedal walker, and to understand how sSNNs may help other more-general agents, we study several simple sensorimotor models driven by sSNNs and present four sSNN functions. Furthermore, we propose that spike-induced ordering is manifested as the spatiotemporally coordinated motion of a bipedal walker, such as the smooth and stable gait (re)initialization and robust balancing.

Results

Model of a Spike-Based Sensorimotor Agent. Because the parameters of sSNNs and conventional nonspiking neural networks (NS-NNs) are substantially different (e.g., time constants, stochasticity, and the nonlinearity of the activation function), simple

Significance

The functional advantages of using a stochastically spiking neural network (sSNN) instead of a nonspiking neural network (NS-NN) have remained largely unknown. We developed an architecture which enabled the parametric adjustment of the spikiness (i.e., impulsive dynamics and stochasticity) of the sSNN output and observed that stochastic spikes instantaneously induced the ordered motion of a dynamical system. We demonstrated the benefits of sSNNs using a musculoskeletal bipedal walker and, moreover, showed that the decrease in the spikiness of motor neuron output leads to a reduction in adaptability. Stochastic spikes may aid the adaptation of a biological system to sudden perturbations or environmental changes. Our architecture can easily be connected to the conventional NS-NN and may superimpose the on-site adaptability.

Author contributions: S.Y. and Y.K. designed research; S.Y. performed research; S.Y. contributed new reagents/analytic tools; S.Y. analyzed data; and S.Y. and Y.K. wrote the paper.

The authors declare no competing interest.

This article is a PNAS Direct Submission.

Data deposition: The source codes used to generate the results in this paper are available at http://www.isi.imi.i.u-tokyo.ac.jp/public/spike_induced_order/.

[1]To whom correspondence may be addressed. Email: yonekura@isi.imi.i.u-tokyo.ac.jp or kuniyosh@isi.imi.i.u-tokyo.ac.jp.

This article contains supporting information online at https://www.pnas.org/lookup/suppl/doi:10.1073/pnas.1819707117/-/DCSupplemental.

First published May 19, 2020.

comparisons of benchmark scores of sSNNs and NS-NNs would not provide sufficient understanding of the functions of stochastic neural spikes; it would be challenging to distinguish the effect of stochastic spikes from that of other parameters. To investigate the functions of stochastic spikes, we considered a sensorimotor agent driven by sSNNs which convert the smooth signal generated by a base controller into the correspondent spike trains, as shown in Fig. 1*A*. Employing this architecture enables the modulation from stochastic and discontinuous sSNN behavior to conventional rate-coded NS-NN behavior by altering PSP timescale and sSNN size (altering these parameters is roughly correspondent to changing the parameters of a lowpass and an averaging filter, respectively) as described later (Fig. 1 *C* and *D*).

The ith sSNN S_i in Fig. 1 consists of N stochastic leaky integrate-and-fire (LIF) neurons, and each neuron in S_i receives a common input signal $I_i(t)$ from a base controller (such as a conventional feedback controller). Furthermore, the jth neuron (in the ith sSNN) receives independent bias input b_{ij} and Gaussian noise $D_i\xi_{ij}(t)$, where D_i indicates the intensity.

As a synapse connecting an sSNN neuron and an actuator, we assumed the simplest linear synapse model (6, 13–15). Then, the activation level $A_i(t)$ of the ith actuator, which is coupled with the ith sSNN, is determined by the total PSP $y_i(t)$ as

$$\tau_s \dot{y}_i = -y_i + \frac{1}{N}\sum_{j=1}^{N}\sigma_{ij}(t), \qquad \textbf{[1a]}$$

$$A_i(t) = g_i^A y_i(t) - A_i^0, \qquad \textbf{[1b]}$$

where $\sigma_{ij}(t)$ is the spike train of the jth LIF neuron, τ_s is the PSP timescale, and g_i^A is the amplification gain to convert excitatory PSP (EPSP) to the activity of an actuator. A_i^0 is the offset inhibition, and $A_i^0 = 0$, unless otherwise stated. Note that A_i is basically positive (although A_i may be offset by A_i^0); therefore, the actuator driven by an sSNN can generate only unidirectional output.

It is important to note that N does not influence $\langle y(t)\rangle$ (where the operator $\langle\cdot\rangle$ denotes the averaging over simulation trials) or $\overline{y} = \int y(t')dt'$, but influences only the variance of y if each spike train of different neurons is independent. [Note that some input may break the independency of each neuron activity as a strong common input inducing the neural synchronization (16, 17)]. Fig. 1*D* shows that N does not change $\overline{y}$ and changes only the variance of y (we used $I = 5$, $b = 4$, $D = 10$, and $\tau_s = 5$ ms). Moreover, the stochasticity and discontinuity of the PSP signal are clearly scaled by the PSP timescale τ_s. Hereafter, we discuss how N and τ_s scale the smoothness and stochasticity of y and approximate the sSNN output to the rate-coded signal. For further discussions, we introduce the variable Z, representing the mean magnitude of spikiness during a certain period $t = [t_0, t_0 + T]$ as follows:

$$Z = \left(\frac{1}{T}\int_{t'=t_0}^{t'=t_0+T}\left(\ddot{y}(t')\right)^2 dt'\right)^{1/2}. \qquad \textbf{[2]}$$

Of note, Z can represent the stochasticity and discontinuity and, therefore, can be a good index for distinguishing an sSNN and a conventional rate-coded neuron network. Using Gaussian approximation of the spike trains of a neuron ensemble (18, 19) and linear-response techniques (6, 20, 21), we can show that $Z \propto 1/\left(\sqrt{N}\tau_s^2\right)$. In fact, Z can be modulated by both the sSNN neuron size, $\sqrt{N}$, and the PSP timescale, τ_s, as shown in Fig. 1*C*. See *Materials and Methods* for details.

Hereafter, we use N and τ_s to parametrically morph the sSNN output to a conventional rate-coded neuron model. Besides the modulation of spikiness, the PSP timescale τ_s plays a special role, described in detail in later sections of the text. Furthermore, it is important to note that modulating τ_s does not influence the total amount of actuator activation $\langle\int_0^\infty y_i\,dt\rangle$ (*SI Appendix*, section S1).

An sSNN-Driven Musculoskeletal Bipedal Walker. We demonstrate how stochastic spikes generated by sSNNs are integrated into the adaptability of a bipedal musculoskeletal system. The configurations for muscle–tendon units (MTUs), a bipedal model, and a reflexive control system are based on ref. 22, as shown in Fig. 2*A*. The smooth nonspiking input to the ith sSNN, $I_i(t)$, is

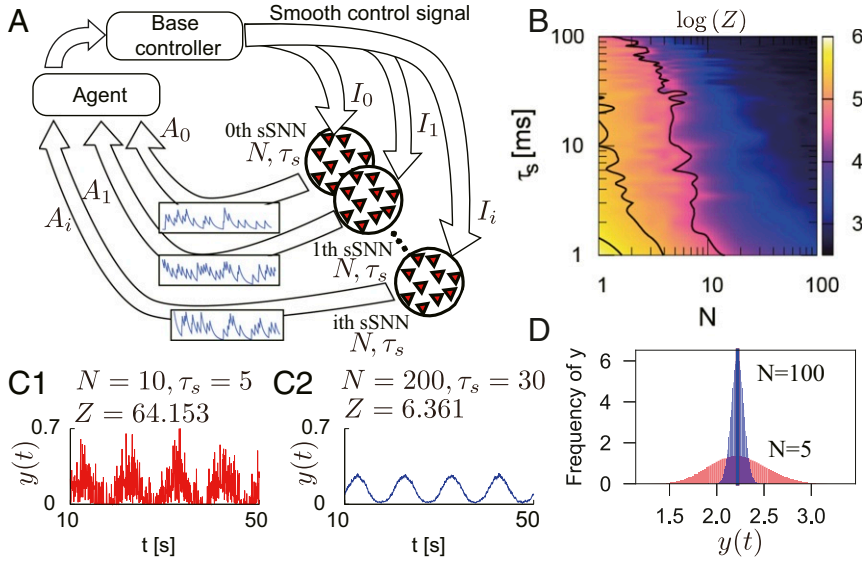

Fig. 1. (*A*) Schematic model of a spike-based sensorimotor agent for seamless modulation from spiking signals to nonspiking, rate-coded signals by altering PSP duration and sSNN size. The neurons in an sSNN receive common (smooth) input and convert the smooth signal to a stochastic spike train. An agent is controlled based on the PSP generated by the sSNNs. (*B*) Spikiness with respect to N and τ_s. The spikiness decreases and approaches the smooth, rate-coding signal as N and τ_s increase. (*C1* and *C2*) The PSP signals are induced by the periodic input $I(t)$ of 0.1 Hz with $N = 10$ and $\tau_s = 5$ ms and $N = 200$ and $\tau_s = 30$ ms, respectively. (*D*) The histogram of y in response to $I = 5$. The average values are the same: 0.66606 with $N = 5$ and 0.66600 with $N = 100$.

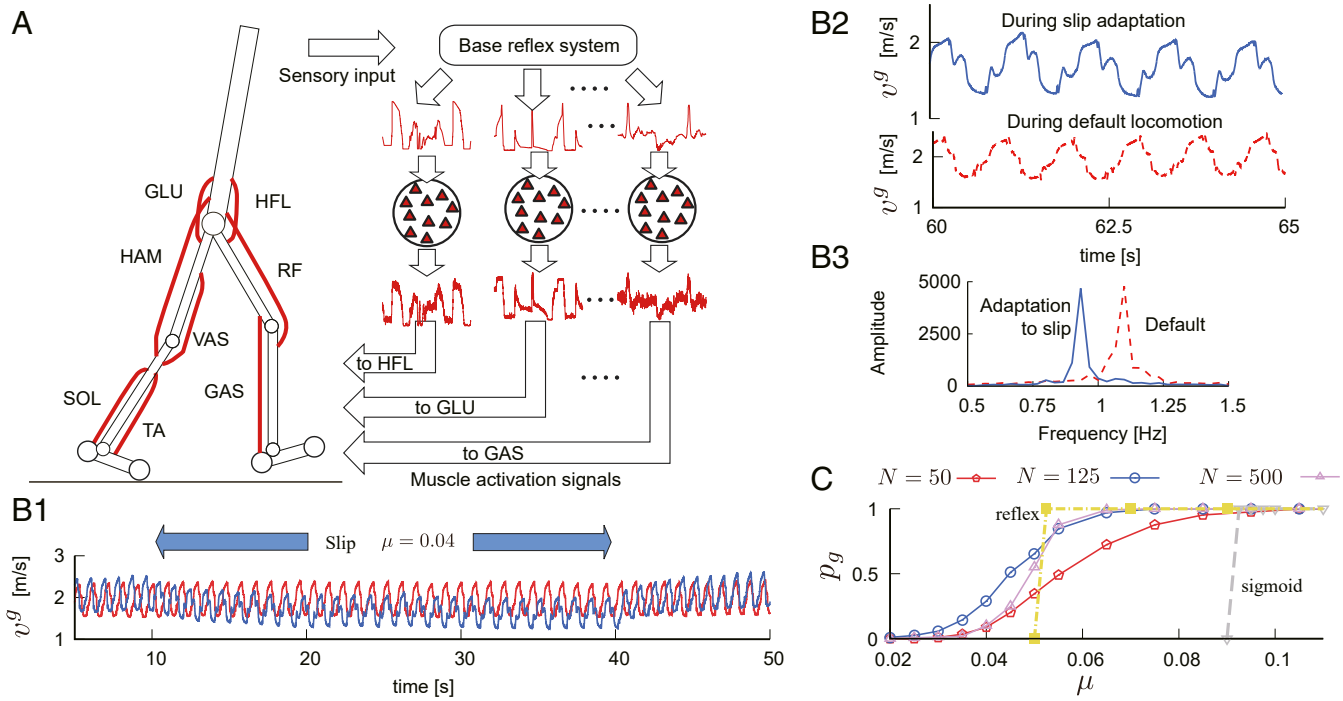

Fig. 2. An sSNN-driven musculoskeletal system of a bipedal walker. (*A*) The bipedal walker consists of 16 muscle–tendon units (MTUs) in total, and the activity of an MTU is determined by the corresponding sSNN, which converts the smooth control signal of a reflex system to an impulsive PSP. We considered the hip flexor muscle group (HFL), the gluteus muscle group (GLU), a biarticular hamstring muscle group (HAM), the femoris muscle group (RF), the vasti muscle group (VAS), the soleus muscle (SOL), the gastrocnemius muscles (GAS), and the tibialis anterior muscle (TA). (*B1*) The sSNN-controlled walker can realize the instant walking rhythm reformation in an extremely slippery environment $\mu = 0.04$. Results are shown for v^g in the environment where the friction coefficient is shifted from $\mu = 10$ to $\mu = 0.04$ during $t = [10, 40]$ (blue line) and in the default environment where the friction coefficient is constant and $\mu = 10$ (red line). The frequency of walking rhythm changes in response to slipping, as shown in *B2*. The numerical simulation was obtained using an sSNN with $N = 125$ and $\tau_s = 5$ ms. (*B2*) Enlarged view of v^g during slip and nonslip walking. The sSNN-driven agent can slow down and reform the walking rhythm in response to slipping, as shown in *B3*. (*C*) Successful gait-initiation ratio p_g of reflex, sigmoid, and sSNN controllers (with $\tau = 5$ ms and several different *N* values) in a slippery environment for $x = [1.25, 5]$.

computed using the reflex rules proposed in refs. 22 and 23 and then passed to the corresponding ith sSNN. The MTU activity A_i is innervated by the EPSP induced by the corresponding neuron ensemble (Eq. **1**), and the generative force of an MTU is computed based on the dynamics proposed in ref. 23.

A conventional sigmoid-type controller and a simple reflex controller are prepared to compare the experimental results. We use the real-coded genetic algorithms (GAs) using a blend crossover α (BLX-α) method (24) to optimize the controllers.

Dynamic Walking Rhythm Formation during Slipping. Bipedal locomotion in a slippery environment requires an agent to decrease the stride frequency. In fact, it is reported that the stride rate in submaximal skating is less than 1 Hz (25) whereas the stride rate during normal walking is usually greater than 1 Hz (26). Because the reflex-based controller involves passive-walking dynamics during the swing phase (23), the original reflex-based controller has the potential ability to adaptively alter the locomotion rhythm in response to environmental changes, such as changes in the slope angle. The sSNN controller inherits this potential ability to ensure reformation of the walking rhythm.

Fig. 2 *B1* and *B2* demonstrates that the sSNN can change the walking rhythm in response to the sudden changes in the friction coefficient to $\mu = 0.04$ during the period $t = [10, 40]$ s and $\mu = 10$ otherwise ($\mu = 0.04$ is smaller than that of a banana skin on the floor and mostly similar to a ski on wet snow) (27). Movie S1 demonstrates bipedal walking using an sSNN controller that successfully slows down the rhythm but fails to find a new stable gait pattern. Successful identification of a new stable gait pattern and instantaneous transition to the stable walking pattern are demonstrated in Movie S2. Note that Movies S1 and S2 are obtained using the same parameters. The difference between Movies S1 and S2 can be accounted for by whether the sSNN instantaneously found and transitioned to the new stable gait.

The sSNN ability for the instant rhythm formation becomes most pronounced in an experiment where a walker is required to initiate a stable gait in a slippery environment; a walker experiences slipping within the first few steps and is required to realize the drastic state transition from a static standing state to a dynamic and stable locomotion gait while preventing falling by slip. Movies S3 and S4 demonstrate that the sSNN controller can slow down the timing of the leg swing in response to the slip of the stance leg and prevent falling, while the reflex-based controller fails to change the walking rhythm, resulting in falling. We used $\mu = 0.04$ for $x = [1.25, 5]$. The successful gait-initiation rate p_g in this environment is shown in Fig. 2*C*. Note that $p_g = C_{suc.}/C_{tot.}$, where $C_{suc.}$ is the number of trials the walker successfully initiated the gait and kept walking during 20 s, and $C_{tot.} = 500$ is the number of total trials. The reflex and sigmoid controllers exhibited a threshold-like behavior in response to μ; the reflex and sigmoid controllers required $\mu \geq 0.05$ and $\mu \geq 0.09$, respectively, to realize gait. The sSNN controller largely relaxed this threshold-like constraint and realized a locomotion with a smaller friction coefficient $\mu < 0.04$. It is also shown that there was an optimal neuron ensemble size N to maximize the adaptability to slipping; $N = 125$ has greater adaptability than $N = 50$ or $N = 500$. To obtain Fig. 2*C*, we first collected the sigmoid and reflex controllers satisfying the optimization cost $J < 0.2$ and then selected the controllers that had the highest successful gait-initiation rate.

Emergent Well-Coordinated Motions. The sSNN-driven walker sometimes exhibits athletic and well-coordinated motion, depending on the initial simulated states. Movie S5 and *SI Appendix*, Fig. S1*A* demonstrate that the sSNN-driven walker tolerates the extremely long-term and long-distance slipping of approximately 0.5 s and 0.5 m slipping. Furthermore, the sSNN-driven walker can recover from the near-falling state if the walker reaches the end of the slippery surface and can have a contact with the nonslippery ground, as shown in Movie S6 and *SI Appendix*, Fig. S1*B*. Skating-like motion, that is obtained using the different parameters of the reflex system and sSNN from other movies, on slippery ground with $\mu = 0.1$, is demonstrated in Movie S7.

Adaptability to External Random Force Perturbation. To further investigate the adaptability of the system, we examined the falling-prevention ratio p_F when a random perturbing external force was applied: Every 0.25 s, the agent upper body receives an external force $F_{ext} = F_0 + F_D\xi_F$ with a probability of $1/4$, where F_D is the noise intensity and ξ_F is a value sampled every 0.25 s from a Gaussian distribution (i.e., with a probability of $3/4$, $F_{ext} = 0$; note that F_{ext} is constant for 0.25 s and is updated to a new value every 0.25 s). We compute p_F using 100 trials of 30-s numerical simulations.

Adaptability Provided by Spikiness. The results shown in Fig. 3*A* demonstrate that the short PSP duration $\tau_s = 2$ ms with a limited neuron ensemble size $N < 100$ is associated with very high adaptability. It is worth noting that the graph for fall-prevention ability with respect to N and τ_s is highly similar to the graph of spikiness shown in Fig. 1*C*. This result clearly implicates that spikiness plays an important role in the ability for instant adaptation.

Furthermore, an sSNN controller exploiting spikiness outperformed a reflexive controller and a sigmoidal controller in the falling-prevention task, as shown in Fig. 3*C*; the admissible force load of an sSNN controller (with $N = 30$ and $\tau_s = 2$ ms) was fivefold and twofold larger than that of a sigmoidal and a reflex controller, respectively (i.e., the maximum force load for an sSNN, a sigmoid, and a reflex controller was 110, 18, and 50 N, respectively). The procedure to select the sigmoidal/reflex controller used in Fig. 3*C* is the same as that to obtain Fig. 2*C*. Note that the reflex controller has a higher falling-prevention ratio than the sigmoidal controller. This might be because the sigmoid controller could not generate the large MTU activation necessary to prevent falling due to the saturation dynamics.

Adaptability Provided by Optimal PSP Timescale. The fall-prevention probability shown in Fig. 3*B* is only weakly dependent on the neuron ensemble size N, while the PSP timescale τ_s is of critical importance for the ability to stabilize. In Fig. 3*B*, $\tau_s : [15, 30]$ ms maximizes stabilization during walking, and the rate of fall prevention is almost insensitive to the size of N. In fact, stability is not reduced or enhanced in the rate-coding regime, such as when $N = 1{,}000$. This result implies that an sSNN can produce adaptability within the musculoskeletal system of a bipedal walker based on principles other than spikiness. Furthermore, Fig. 3*B* implies the existence of an optimal PSP timescale τ_s to maximize adaptability.

Analyses Using Simple Sensorimotor Agents. Balancing of a standing biped system is often modeled using an inverted pendulum on a ground (28, 29) supported by passive torque generated by the ankle joint stiffness. Such a system has a bistable potential function as $V(x) = \cos(x) + kx^2$, where x is the scaled pendulum angle and k is a spring coefficient (30, 31), and increasing the muscle coactivation at the ankle or hip joint increases the joint stiffness k and improves the posture stability (32, 33). Gait (re)initiation from the initial posture or the near-falling state requires a transition from the such-stabilized (and rather rigidized) posture to a dynamical and periodic alternation of joint posture such as forward–backward swinging of the upper body (34, 35). Furthermore, to improve energy efficiency and locomotion stability, the periodic motions of an upper body or a swinging leg must match the natural frequency of a passive mechanical system (23, 36, 37). Bipedal walking and recovery from the near-falling state require solving these issues. Hereafter, we discuss how sSNNs help an agent achieve these subtasks by using several simplified abstract models.

Synchronization to the Natural Frequency. We start our analysis for how sSNNs may help a tight synchronization to the natural frequency (SNF) of a target system. We consider generating the oscillatory motion of a particle connected to a spring, for simplicity, because the mass–spring system has an explicit form of a natural frequency. The motion equation of the spring–mass system is described as $\ddot{x} = -\gamma\dot{x} - kx + (A_0 - A_1) + K_p\,(x_g - x)$, where k is the spring coefficient, γ is the damping coefficient, and $A_{0/1}$ is the force generated by sSNNs. Note that if K_p is as small as $K_p < 1/4\gamma^2$, the system has convergent solution and $x \to x^g$ (with the assumption $A_i = 0$). Likewise, if $K_p = 1/4\gamma^2$, the system exhibits stable periodic behaviors, and for $K_p > 1/4\gamma^2$, the system exhibits periodic and divergent behaviors.

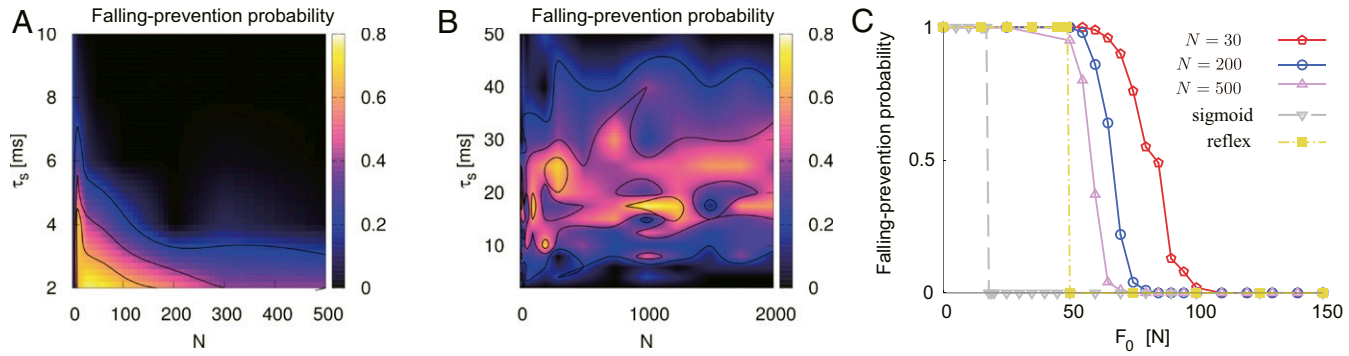

Fig. 3. The falling-prevention ratio p_F in response to an external perturbing force. We found that adaptability manifested in two different ways: Adaptability was significantly improved by spikiness, as shown in *A*. In addition, adaptability was improved by an optimal PSP timescale range, i.e., $\tau_s : [15, 30]$, although these effects were only weakly related to the neuron ensemble size *N* (*B*). (*A*) Adaptability in response to external perturbation is maximized with $N < 100$ and $\tau_s < 5$ ms, exhibiting strong similarity to the graph of spikiness shown in Fig. 1*B*. We used $F_0 = 50$ N and $F_D = 100$ N. (*B*) We found another parameter set for which adaptability occurred critically dependent on τ_s and almost insensitive to *N*. We used $F_0 = 30$ N and $F_D = 75$ N. (*C*) p_F of sSNN, sigmoidal, and reflex controllers in response to the stationary force input F_0 to a hip. The sSNN controller used in *A* outperformed the other controllers.

The input and output of sSNNs are designed so that sSNNs generate a periodic oscillatory motion of a spring–mass system; sSNNs form a positional feedback controller where the gains g_s and g^A are adjusted sufficiently large to generate the oscillatory motion of a particle. The input to sSNNs is described as $I_0(t) = g_s\,(x - x^g)$ and $I_1(t) = g_s\,(x^g - x)$. Furthermore, we used the bias input $b = 0.5$ (*SI Appendix*, section S3).

The natural frequency of the spring–mass system is $f_0^\gamma = \sqrt{k + K_p - 1/2\gamma^2}/(2\pi)$ Hz, and the oscillation amplitude of $x(t)$ diverges if the frequency of any external forces matches to f_0^γ. It is clear that introducing the positional feedback gain K_p is equivalent to modulating the spring coefficient k as $k \to (k + K_p)$. Therefore, theoretically, all smooth rate-based feedback controllers inevitably distort the original intrinsic dynamics of a subject system. This is clearly shown in Fig. 4*A*, where we define R_f as the ratio of f, the actual frequency of the oscillatory motion of $x(t)$, and the natural frequency f_0^γ as $R_f = f/f_0^\gamma$. Evidently, perfect synchrony to the intrinsic dynamics gives $R_f = 1$. Fig. 4*B* demonstrates that the sSNN can achieve $\langle R_f \rangle \sim 1$ with a wide range of f_0^γ and g^A. Note that, however, for very low natural frequencies such as $f_0^\gamma \le 0.1$, the neuron time constant τ or PSP time constant τ_s must be adjusted to realize $\langle R_f \rangle \sim 1$. See also *SI Appendix*, Fig. S2 for further analyses for the $\langle R_f \rangle$ dependency on the parameters such as τ and τ_s.

As a subsequent measure to observe the sSNN synchrony to the intrinsic dynamics, we used the signal-to-noise ratio (SNR) around the natural frequency f_0^γ (with $K_p = 0$). The SNR was computed as $\mathrm{SNR} = 10\log_{10}\left(A_s^2/A_n^2\right)$, where the signal power, A_s, is the spectrum amplitude around the f_0^γ, and the noise power, A_n, is computed by subtracting A_s from the total power spectrum. (The SNR was computed using the data obtained during $t = 200$ to 500 s.) The resonant motion of a mass–spring system is generally evaluated from the maximum amplitude of the induced oscillatory motion. However, the maximum amplitude of the motion cannot discriminate resonances in the natural frequency and in the frequency distorted by a smooth controller. Therefore, we used SNR such that only the resonant motions in the natural frequency will result in high SNR.

PSP Resonance: Resonance Amplitude in Natural Frequency Is Modulated by PSP Time Constant. Fig. 5 shows the graphs of SNR for several natural frequencies f_0^γ and neuron time constants τ with respect to the PSP timescale τ_s. These graphs indicate that sSNNs can induce resonant motion (i.e., SNR > 0) with a significantly wide sSNN parameter range. Furthermore, Fig. 5 *A* and *B* indicates an interesting characteristic of sSNNs: SNR drastically changes by a small difference of τ_s. It is shown that W_s, i.e., the width of τ_s for the SNR peak (see Fig. 5*B* for the schematic explanation of what W_s indicates), increases corresponding to the range of τ_s. For example, the W_s (for f_0^γ = 3) was <0.2 s for the peak around $\tau_s \approx 1.2$ s, and for the peak around $\tau_s \approx 6$ s, W_s increases to ~ 2 s. Furthermore, Fig. 5*B* shows that the resonance peak positions are different for the different values of f_0^γ; e.g., the peaks for $f_0^\gamma = 3$ are given by $\tau_s = \{22, 31, \ldots, 400, 600, 1{,}200, 6{,}000\}$ ms, and the peaks for $f_0^\gamma = 5$ are given by $\tau_s = \{8.5, 9.5, 11, \ldots, 520, 2{,}100\}$ ms (*SI Appendix*, Fig. S3).

To summarize, sSNNs do not distort the intrinsic dynamics of a system unlike the conventional smooth rate-based controllers, and therefore an sSNN-based motion controller would be more suitable for exploiting profoundly more mechanical intrinsic dynamics. For example, the locomotion rhythm change in slipping shown in Fig. 2 would be accounted for by SNF; in slipping, the potential of a mechanical bipedal system is reduced from $V(x) = \cos(x) + kx^2$ to $\cos(x)$ because the ankle support drops so that $k \sim 0$, and therefore the natural frequency of the system is modulated by slipping. Furthermore, we observed a locomotion gait where the agent swings the legs and the upper body largely as shown in Movie S8, which is very similar to passive dynamic walking (38). This gait is used to obtain the result in Fig. 3*B*, and therefore this gait stability is mostly dependent on the PSP timescale τ_s and only weakly sensitive to the sSNN size N. This gait pattern might be realized using the SNF and PSP resonance.

Enlarging the Basin of a Goal State. Here, we analyze how sSNNs help bipedal balancing in a near-falling state. Because the bipedal system is analogously represented by a spring-supported inverted pendulum (30, 31) which has a double-well potential, we consider the particle agent in a double-well potential as shown in Fig. 6*A*. The motion equation is described as $\ddot{x} = -\gamma\dot{x} - \partial_x V(x) + (A_0 - A_1) + H(x,t)$; γ is a friction coefficient, and ∂_x denotes differentiation with respect to x. Note that we consider a more mathematically generalized double-well potential $V(x) = 1/4x^4 - 1/2x^2$.

The sSNNs are configured to compose a feedback controller to reach the potential top $x_g = 0$. The inputs to S_0 and S_1 are $I_0(t) = g_s\,(x^g - x)$ and $I_1(t) = g_s\,(x - x^g)$, respectively. The

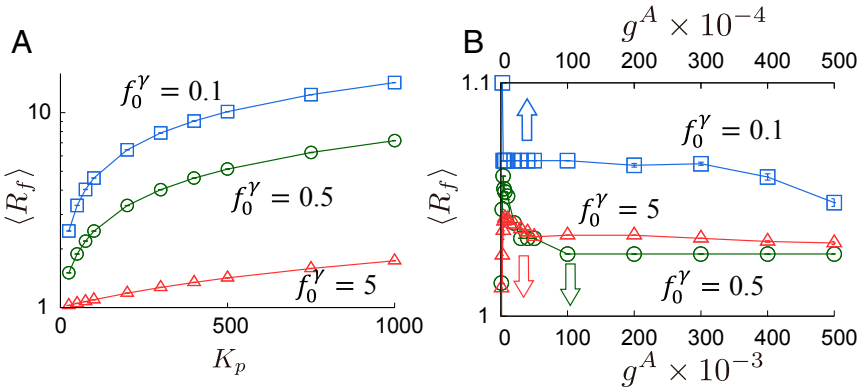

Fig. 4. The comparison $R_f = f/f_0^\gamma$ using the conventional feedback controllers versus sSNNs. (*A*) $\langle R_f \rangle = f/f_0^\gamma$ obtained using a conventional feedback controller with $x_g = 0$. Note that increasing controller gain K_p distorts the motion frequency apart from the natural frequency f_0^γ. (*B*) $\langle R_f \rangle$ obtained using an sSNN controller. $\langle R_f \rangle$ is only weakly sensitive to the changes in the controller gain g^A, unlike the conventional feedback controller. The R_f was computed using the data obtained during $t = 200$ to 500 s, and $\langle R_f \rangle$ was obtained by averaging the 1,000 simulation trials with $\gamma = 1$. We used $\tau = 5$ s, $\tau_s = 10$ s, $g_s = 50$, and $D = 3{,}000$ for $f_0^\gamma = 0.1$ Hz; $\tau = 500$ ms, $\tau_s = 500$ ms, $g_s = 5$, and $D = 1{,}500$ for $f_0^\gamma = 0.5$ Hz; and $\tau = 10$ ms, $\tau_s = 100$ ms, $g_s = 1$, and $D = 15$ for $f_0^\gamma = 5$ Hz. Note that $\langle R_f \rangle$ for $f_0^\gamma = 0.1$ Hz corresponds to the upper *x* axis.

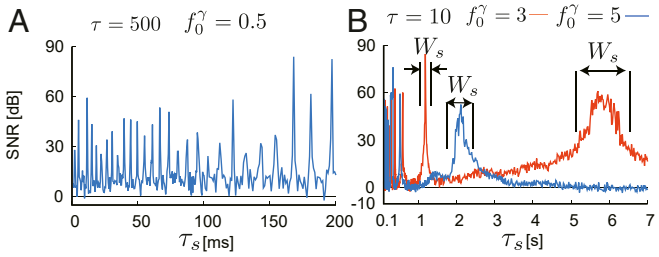

Fig. 5. (*A* and *B*) SNR with respect to τ_s, f_0^γ, and τ. *A* and *B* show that a stochastic spiking controller can generate resonance in the natural frequency of a system using a wide variety of parameter regions (i.e., SNR >0 for a wide range of τ_s). Additionally, it should be noted that the value of SNR is further amplified by optimal values of τ_s. Here, we used $\gamma = 1$, $g_s = 1$, $b = 0.5$, $D = 15$, $g^A = 5 \times 10^5$, and $N = 10$. These results are only weakly sensitive to the changes in N (*SI Appendix*, Figs. S2 and S3).

controller gains g_s and g^A were designed small so that the agent which started from the potential bottom $x = \pm 1$ could not reach x_g. The output of an sSNN controller is approximately sigmoidal with respect to the agent position x, as shown in Fig. 6*B*. We prepare a stochastic feedback controller for comparison; $H(x,t) = -K_p x + D_f \xi_f(t)$, where K_p is the control gain and $D_f \xi_f(t)$ is the Gaussian random perturbation with the intensity D_f. Note that $H(x,t) = 0$ when we use sSNN controllers. For the detailed description of the controller setup, see *SI Appendix*, section S4).

Fig. 6 *C1* demonstrates that $H(x,t)$ cannot stabilize the agent around $x = 0$ even with the external help that is given as v_0 or with the presence of noise $D_f \xi_f$, if K_p is not large enough to lift the agent from $x_\pm = 1$ up to $x_g = 0$. In contrast, Fig. 6 *C2* demonstrates that the sSNN controller induces a metastable state around the goal state and exploits the external help (i.e., v_0) and force noise generated by the stochastic spikes to overcome the potential barrier to reach the goal state. This characteristic helps the agent start from the wider range of the initial state (x_0, v_0) to reach and stay in the goal state. Therefore, we investigate the basin size, which reflects the size of the set of the initial states (x_0, v_0) that enables the agent to reach $x_g = 0$ and stay within $[-0.1, 0.1]$ for a sufficiently long duration, i.e., 30 s.

The basin size is computed as follows: For the mth pair of initial position and velocity $X_m = (x_0, v_0)_m$, we set $B(X_m) = 1$ if the agent succeeds in staying on the ridge $[-0.1, 0.1]$. Otherwise, $B(X_m) = 0$. We define the basin rate S_b as $S_b = \frac{1}{M}\sum_{m=1}^{M} B(X_m)$, where M is the total number of X_m. Fig. 7 *A1* and *A2* represents the basin $B(X_m)$ obtained with $\gamma = 0.5$, $\gamma = 0.1$, respectively. (Note that we set the pixel to 1 if the corresponding initial state $(x_0, v_0)_m$ is a part of the basin.) Fig. 7 *B1* and *B2* indicates the basin area rate S_b computed using several bias input values for b, which determines the mean-firing rate of an sSNN. We observed the tendency of the basin size to decrease with respect to N for most of the b and γ. However, if the friction is low, $\gamma = 0.1$, and if the bias is as small as $b \leq 0$ and the sSNN is in the subthreshold regime (i.e., the sSNN does not generate spikes near $x = 0$), the small N reduces the basin size.

The basin-enlargement phenomenon implies that sSNNs can induce an inhomogeneous noise effect. We speculate that this inhomogeneous noise effect is based on the interaction of the nonlinear firing function $r(z)$ and noise of the sSNNs: In the sSNN suprathreshold regime $b > 0$ (i.e., an sSNN emits spikes without any input I), $\langle \overline{y} \rangle$ can be approximated as $\langle \overline{y}(x) \rangle \approx 6x + 0.3$ for $x \sim 0$, and $\langle \overline{y}(x) \rangle \approx 1.2x + 1.7$ for $x \gg 0$, as shown in Fig. 6*B*. This implies that the diffusive motion of an agent induced by noise is less suppressed if the agent is far from the goal state; $x \gg 0$ but more suppressed near the goal state $x_g = 0$. In the subthreshold regime such as $b \leq 0$, on the other hand, $\langle \overline{y}(x) \rangle \approx 0$ for $x \sim 0$. Therefore, the diffusive motion of an agent is rather uncontrolled near the goal state in the subthreshold regime $b \leq 0$. This would lead to the result where the small N degrades the basin rate with $b = 0$ as shown in Fig. 7 *B2*.

Rapid Complexity Reduction and Rhythm Formation. In gait (re)initialization, a bipedal system must transit from a rigidized posture (that is induced by the muscle coactivations to improve the balance stability) to a dynamical, periodic motion regime. This transition is analogous to escaping from a quasi-stable state and forming a dynamic motion pattern in a multistable potential (note that in such dynamic motion, the quasi-stable state will

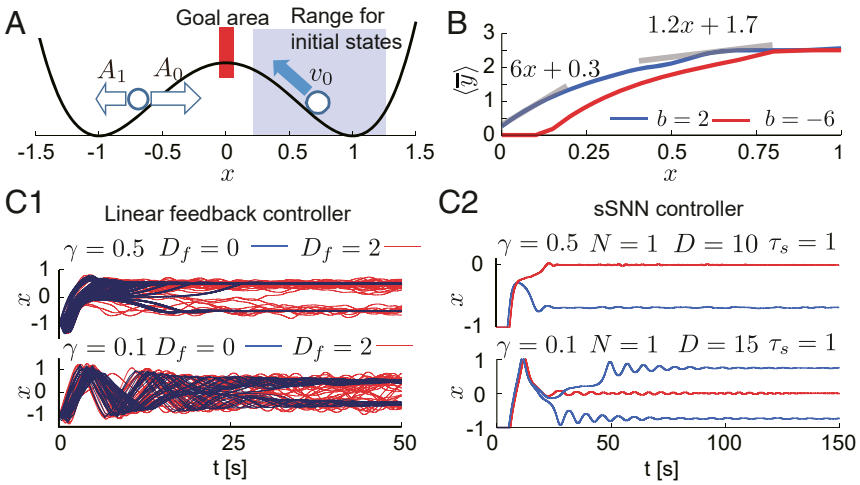

Fig. 6. Stabilization in the goal state by the sSNN controller in a double-well potential. (*A*) Potential landscape and controller setup used in the experiment. See *Enlarging the Basin of a Goal State* for details. (*B*) Time-averaged PSP in response to x. We fixed the particle position and observed the stationary value of $\langle \overline{y} \rangle$. (*C1*) Superimposed particle trajectories obtained with the initial position $x_0 = -1$ with several v_0 values such that $-0.5 \leq v_0 \leq 1$. We used $K_p = 0.75$. The other parameters are listed within the panels. Note that linear feedback controllers cannot stabilize the particle around $x_g = 0$ even if noise intensity is $D_f > 0$. (*C2*) Typical particle trajectory obtained with $\gamma = 0.5$ (*Top*) and with $\gamma = 0.1$ (*Bottom*). In the low-friction environment $\gamma = 0.1$, the particle often overshoots the goal position; the starting agent $x_0 = -1$ overshot the goal and reached $x = 1$, and then it rebounded to reach the goal state. For $\gamma = 0.5$, we used $v_0 = 0.35$, $b = 3$, $D = 10$, $g_s = 10$, and $g^A = 0.3$. Likewise, for $\gamma = 0.1$, we used $v_0 = 0.4$, $b = 4$, $D = 15$, $g_s = 15$, and $g^A = 0.21$.

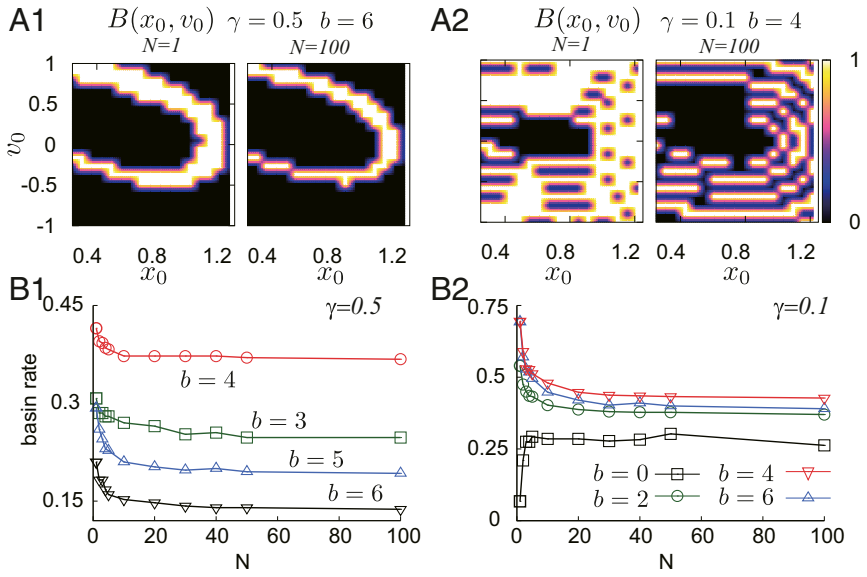

Fig. 7. Basin area rate decreases with respect to *N*. (*A1* and *A2*) The basin plot for the initial state $X_i = (x_0, v_0)_i$ and with $\gamma = 0.5$ (*A1*) and 0.1 (*A2*). Note that the basin size decreases as *N* increases. The several stripes in *A2* reflect the overshooting behavior of the particle (in the low-friction environment, the agent cannot stop at the goal state if v_0 is very large; see Fig. 6 *C2*). (*B1* and *B2*) The basin area rate exhibits monotonic decreases with respect to *N* for $\gamma = 0.5$. If the sSNN bias is small and in the subthreshold regime (e.g., $b \leq 0$), the basin size decreases with small *N*, particularly in the low-friction environment $\gamma = 0.1$ because the spike frequency of sSNN is low and therefore the agent is rather uncontrolled near $x = 0$. See text for further analysis. The parameters used in the simulations are listed in the corresponding panels. For the other sSNN parameters, we used $\tau_s = 1$ ms, $D = 10$, $g_s = 10$, and $g^A = 0.3$ for $\gamma = 0.5$ and $\tau_s = 1$ ms, $D = 15$, $g_s = 15$, and $g^A = 0.21$ for $\gamma = 0.1$.

be destabilized because of the large motion velocity). Here, we considered a particle system in a triple-well potential $V_3(x) = x^6 - 6x^4 + 8x^2$, as shown in Fig. 8*A*.

The motion equation of an agent is given by $\ddot{x} = -\gamma\dot{x} - \partial_x V_3(x) + (F_0 + F_1) + H(x, t)$, where $\gamma = 0.5$ is a friction coefficient, and ∂_x denotes differentiation with respect to x. The sSNN controllers S_0 and S_1 were designed to mimic the function of antagonist muscles; S_0 and S_1 generate forces driving toward two different goal states $x_0^g = -1$ and $x_1^g = 1$, respectively. In particular, we assumed that S_0 received $I_0(t) = g_s\,[x - x_0^g]_+$ and generated $F_0(t) = -A_0(t)$ toward x_0^g. Likewise, S_1 received $I_1(t) = g_s\,[x_1^g - x]_+$ and generated $F_1(t) = A_1(t)$ toward x_1^g. The stochastic feedback controller to mimic the function of antagonist muscles was introduced for the sake of comparison, as $H(x, t) = (B_1 + B_0) + D_F\xi_F(t)$, where $B_i = K_p(x_i^g - x)$ (see *SI Appendix*, section S5 for the detailed controller design). $H(x, t)$ simply increases the stability of the quasi-stable state if $x_0^g = -x_1^g$ as we can see that $H(x, t)$ is reduced to a simple spring-like controller as $H(x, t) = -2K_p x + D_F\xi_F(t)$. Note that this would be corresponding to the increased joint rigidity by muscle coactivation (32, 33). Basically, $H(x, t)$ prevents the smooth transition from the stabilized posture regime to a periodic motion regime without the help of noise, as shown in Fig. 8*B*. In contrast, sSNNs with small N have enhanced escaping from the quasi-stable well $x = 0$ and generate a periodic motion among $x_\pm$ as shown in Fig. 8*C*. Fig. 8*D* indicates that the time required to obtain an oscillatory motion pattern, T_r tends to increase with N, where T_r is obtained by observing the time when the particle finishes passing both of $x_\pm^l$. For relatively small actuator gains such as $g^A = 100$, escaping from $x = 0$ is realized only with a small N such as $N < 50$.

Furthermore, escaping from the quasi-stable well where two controllers generate conflicting forces leads to the complexity reduction. In fact, Fig. 8 *B* and *C* demonstrates that the approximate entropy (ApEn) (39), a measure to quantify complexity, is drastically reduced by escaping from the quasi-stable well. This is because the agent outside the quasi-stable well is influenced more by the deterministic large force generated by the potential $V_3(x)$. (Intuitively, ApEn quantifies the infrequency of the same data pattern in a time series, and therefore regular and periodic time series give small ApEn. See *SI Appendix*, section S6 for the detailed definition of ApEn.) Fig. 8*E* shows a result that smaller neuron sizes N (particularly $N < 100$) can more effectively reduce ApEn than larger neuron size such as $N \geq 500$.

The ability of stochastic spikes to form patterns is similar to the well-established coherence resonance induced by noise (see ref. 6 for review) and noise-induced posture transition (40), and, therefore, similar to sSNNs, a linear controller can achieve a periodic motion if there is the help of noise $D_F\xi(t)$, as shown in Fig. 8*E*.

Discussion

Adaptability Improvement by Spikiness. It is well known that walking requires the zero-moment point (ZMP) (41) to be within a certain range, which (in our framework) mainly corresponds to upper-body control toward and within a certain range. Note that this upper-body control is analogous with the problem formulation introduced in *Enlarging the Basin of a Goal State*. Furthermore, finding and transitioning to a new stable walking pattern upon perturbation must be analogous to rapid pattern formation discussed in *Rapid Complexity Reduction and Rhythm Formation*. Because these functions are enhanced by large spikiness (Figs. 6 and 8), it would be reasonable to say that the fall-prevention ability in response to the slipping, that is maximized by large spikiness, would be largely dependent on the basin-enlargement and complexity-reduction ability.

Adaptability Improvement by SNF and PSP Resonance. Several studies of animal locomotion have proposed that locomotion frequency is generated near the natural frequency of the musculoskeletal system (23, 36, 37). The parameter band

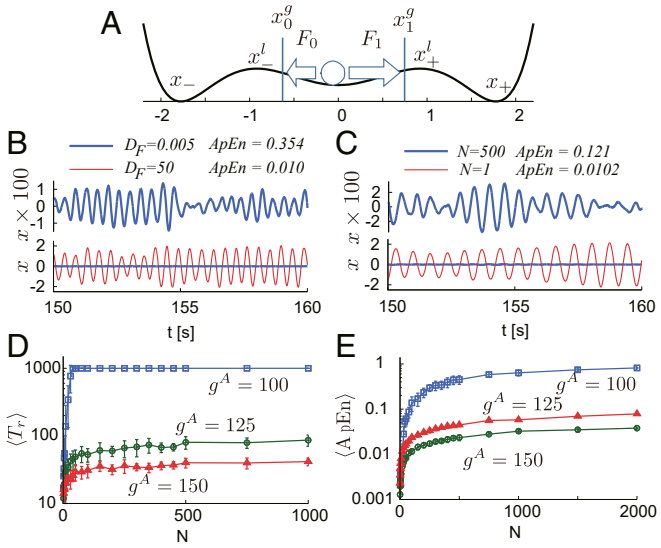

Fig. 8. Rapid complexity reduction due to stochastic spikes. (*A*) Potential landscape and controller setups in the experiment. (*B*) The position trajectories obtained using a stochastic nonspiking controller $H(x, t)$. The noise intensity $D_F = 50$ (*Bottom*) generated a more regular oscillatory motion and resulted in lower ApEn = 0.01, compared with a lower-noise controller with $D_F = 0.005$ (enlarged view in *Top* and *Bottom* in the same scale with $D_F = 50$) (ApEn = 0.354). We used $K = 100$. (*C*) The position trajectories obtained by using the sSNN controller with $N = 1$ (*Bottom*) and $N = 500$ (enlarged graph in *Top* and the same scale with $N = 1$ in *Bottom*). We used $\tau_s = 5$ ms, $g^A = 100$, $b = 0.3$, $D = 15$, and $g_s = 4$. (*D*) Averaged time $\langle T_r \rangle$ with respect to N and actuation gain g^A. Note that $\langle T_r \rangle = 1{,}000$ indicates that the agent could not escape the local minimum. (*E*) ApEn with respect to N and several actuation gains. ApEn increases with N for a wide variety of g^A values. The ApEn values were calculated using the data obtained during $t = 150$ to 1,000 s. *D* and *E* were computed by averaging the results of 50 trials of numerical simulations performed using the equations $x_0^g = -1$, $x_1^g = 1$, $\tau_s = 5$ ms, $b = 0.3$, $D = 15$.

$\tau_s : [15, 30]$ that realizes high falling-prevention probability would correspond with the PSP resonance band shown in Fig. 5. One interpretation for the parameter band $\tau_s : [15, 30]$ would be that sSNNs exploited the musculoskeletal natural frequency by SNF and stabilized the rhythmic motion by PSP resonance.

Why Most Biological Systems Rely on Spiking Neurons. Even the unicellular *Paramecium* use the action potential to generate behavior (42). Although biological organisms contain a few types of nonspiking interneurons (43–46), sensory information and motor activation are mainly regulated by spiking action potentials in biological systems. Recent developments of neuromorphic chips have revealed that learning systems using spiking neurons can solve optimization problems with remarkably higher-power efficiency (47–49). Nevertheless, the merits of biological spiking neurons remain to be fully elucidated. In fact, state-of-the-art, biologically inspired engineering frameworks such as deep learning (50), deep reinforcement learning (51), and their derivatives still employ nonspiking rate-based neurons because spiking neurons have not yet been associated with any remarkable benefits in learning and optimization ability other than the computational efficiency.

Our findings suggest that the merits of spiking action potentials are beyond the scope of the conventional framework for learning: We believe that the functions of spiking neurons must be within the scope of emergent adaptability and instantaneous behavioral optimization. Moreover, we deduce that the emergent adaptability would increase the chances of success in a sensorimotor task and therefore enable a smooth and rapid sensorimotor learning process.

An sSNN to Realize a Brownian Ratchet in Large-Scaled Systems. Our results imply that the sSNNs can provide the inhomogeneous noise effect to a musculoskeletal system; the force noise generated by sSNNs helps an agent overcome the potential barrier to reach a goal state for a certain task, and simultaneously, a control signal to prevent the force noise from pushing the agent from the goal state is provided by the nonlinear firing function of an sSNN. Similar adaptive and autonomous switching between exploiting and blocking the noise effect is seen in a model of neural dendrosomatic interaction (52). An sSNN may be a key platform to realize a Brownian ratchet-like mechanism (53, 54) in a large-scaled system such as animal musculoskeletal systems where the effect of thermal noise is negligible. A theoretical analysis must be necessary for further understanding of this ratchet-like behavior of sSNNs.

From the Perspective of Spike-Induced Ordering. Animal skeletal muscle groups are controlled by a limited number of motor neurons. For example, the motor axons of a human skeletal muscle group (such as the tibialis anterior muscle [TA], which consists of more than 250,000 muscle fibers) are controlled by at most 500 neurons (55). This indicates that the PSP signals induced in a muscle group are principally not smooth and are very far from the perfect rate-coding scheme. Our experimental results suggest that jerking and spiking MTU control signals lead to adequate complexity reduction and basin enlargement, as shown in Figs. 3*A*, 6, and 8. These results provide insight into why most animal skeletal muscles are innervated by a limited number of neurons: Motion control by a limited number of neurons may extend beyond the economical purpose of minimizing the control cost and act to exploit the effect of spike-induced ordering. Furthermore, we expect that the target function of spike-induced ordering is not limited to musculoskeletal motion control and may be applicable to the homeostatic regulation of endocrine systems, ordered peristalsis motions of digestive organs, and ordered respiratory dynamics.

From the Perspective of SNF and PSP Resonance. In biological systems, the duration of an action potential (AP) is tightly coupled to the PSP duration and amplitude (56, 57). Therefore, we speculate that the effects induced by modulating the PSP timescale as demonstrated in this paper may be applicable to the effects induced by modulating AP duration. In particular, we hope that our results provide a theoretical basis as to why the AP duration in biological systems differs, depending on the neuron type and target function (56). Furthermore, we speculate that one of the functionalities of neuromodulators such as noradrenaline (NA), acetylcholine, and serotonin (5-HT) may be in the controlling AP waveform and duration, and PSP time constant (58–61), to synchronize with the system's intrinsic dynamics. In fact, it is known that NA in a respiratory CPG modulates the respiration frequency (62). Likewise, 5-HT in the spinal central pattern generators (CPGs) is required to generate stable locomotion pattern (63). We further expect that the effects of PSP resonance must not be limited to the generation of rhythmic motion and may play a certain role in the formation of rhythmic brain activity, e.g., α, β, γ, and δ oscillations.

Note that an sSNN described in this paper does not contain any synaptic connection among the neurons in an ensemble. We point out that several computational models for spinal and respiratory CPG circuits (64, 65) are based on the same assumption: A neuron population consisting of 50 to 100 spiking neurons does not involve any synaptic connection within a population and has synaptic interconnection only with other neuron populations.

Conclusion

In this study, we investigated the function of stochastic spikes with respect to the spikiness and PSP timescale. We reported four findings (F1 to F4) regarding the benefits of stochastic spikes: F1) synchronization to an intrinsic frequency, F2) amplification of the resonant motion in a natural frequency by PSP timescale, F3) basin enlargement, and F4) rapid complexity reduction and pattern formation. We demonstrated that the integration of these four functions leads to the on-site adaptability of a sensorimotor agent. We further observed that F3 and F4 are roughly correlated with the level of spikiness, while F1 and F2 are correlated with PSP timescale. Artificial intelligence systems developed using stochastic spikes may exhibit substantial differences in adaptability when compared with conventional systems engineered using nonspiking neuron models.

Data Availability. The source codes used to generate the results in this paper are available at http://www.isi.imi.i.u-tokyo.ac.jp/public/spike_induced_order/.

Materials and Methods

A Model of Stochastic LIF Neuron Ensemble. The membrane voltage of the jth neuron (in the ith sSNN) is represented by v_{ij}, and when v_{ij} reaches the threshold v^θ ($v^\theta = 20$ throughout this paper), the neuron emits a spike represented by the Dirac delta function δ and enters a refractory period described by τ_{ref}. Simultaneously, the membrane voltage is reset to v_{ij}^R. Formally, the full dynamics of an LIF neuron can be described as (66)

$$\tau \dot{v}_{ij} = -\gamma v_{ij} + b_{ij} + I_i(t) + \sqrt{2D_i}\xi_{ij}(t), \quad [3a]$$

$$v_{ij} = v^\theta \Rightarrow t_{ijk} := t,\ v_{ijk}(t + \tau_{ref}) = v_{ij}^R, \quad [3b]$$

$$\mathcal{T}_{ij} = \{.., t_{ijk-1}, t_{ijk}, t_{ijk+1}, ..\}, \quad [3c]$$

where b_{ij} is the bias current, D_i is the noise intensity of the ith sSNN, τ_{ref} is the refractory period, $\tau_{ref} = 2$ ms, ξ is the Gaussian noise of the unit intensity, and τ is the membrane time constant and $\tau = 10$ ms unless otherwise stated. ξ represents the noisy synaptic background activity (6, 66, 67) and is the source for the stochasticity of an sSNN. Note that we use the suffixes i, j, and k to represent the sSNN index, the neuron index, and the spike index, respectively. The spike train of the jth LIF neuron is formally described as $\sigma_{ij}(t) = \sum_{t_{ijk} \in \mathcal{T}_{ij}} \delta(t_{ijk} - t)$ (6). The v_{ij}^R and b_{ij} are different for different neurons and are randomly sampled from the range $V_i^R : [v_{min}^R, v_{max}^R]$ and $B_i : [b_{min}, b_{max}]$, respectively. Note that the ith sSNN has each independent profile for D_i, V_i^R, and B_i, and $I_0, I_1, \ldots$ are independent of each other. Furthermore, we used different b_{ij} values for different neurons in an ensemble in our numerical simulations of a musculoskeletal bipedal walker, and we used the same bias signal $b_{ij} = b$ in the numerical simulations of simplified sensorimotor agents.

Main Idea: Parametric Control of the Stochasticity and Discontinuity of sSNN Output. To simplify the theoretical analysis, we assume that the b_{ij} are identical for all neurons in the same sSNN as $b_{ij} = b_i$. Based on the finite-size mean-field theory developed in refs. 18 and 19 and linear-response theory (6, 20, 21), the averaged spike train can be described using Gaussian approximation as

$$\frac{1}{N}\sum_{j=1}^{N} \sigma_{ij}(t) \approx r(b_i + I_i(t)) + \sqrt{\frac{1}{N}}\eta_i(t), \quad [4a]$$

$$\approx r_0(b_i) + \sum_\omega G(\omega) s(\omega, t) + \sqrt{\frac{1}{N}}\eta_i(t), \quad [4b]$$

where, $r(x)$ is a certain firing function, r_0 is the stationary firing rate, and $G(\omega)$ is the linear-response function. $I_i(t)$ consists of several periodic signals such as $I_i(t) = \sum_\omega s(\omega, t)$ (21). We used a simplified approximation that the spike train of a LIF neuron is based on the Poisson process and assumed that $\eta_i(t)$ is Gaussian white noise of the variance $r_0(b_i)$ (6). Note that η_i has a scaling factor of $\sqrt{N}$ rather than N because of the independency of σ_{ij} and $\sigma_{ij'}$; i.e., $\int_0^\infty \sigma_{ij}(t)\sigma_{ij'}(t)dt = 0$ ($j \neq j'$). Note that to be theoretically exact, however, it is shown that $\eta_i(t)$ is nonwhite but colored because of the LIF refractory period and membrane dynamics (18, 19). The plot of $r(x)$ and $r_0(x)$ mostly takes a sigmoidal shape with respect to the input x (6, 20), providing an activation function similar to that used in conventional nonspiking neural networks.

Using the abovementioned approximation of σ_{ij} in Eq. **4**, the dynamics of $y_i(t)$ in Eq. **1** are approximated as follows:

$$\tau_s \dot{y}_i \approx -y_i + r_0(b_i) + \sum_\omega G(\omega) s(\omega, t) + \sqrt{\frac{1}{N}}\eta_i(t). \quad [5]$$

Eq. **5**, which is obtained by substituting Eq. **4** for Eq. **1**, implies that the PSP signal generated by the output spikes of the sSNN asymptotically approaches the rate-coded smooth behavior and that this asymptotic scaling is primarily based on $\sqrt{N}$. If the PSP signal $y(t)$ can be expressed similarly to Eq. **5** as

$$y_i(t) = Y_0(b_i) + \sum_\omega \mathcal{F}(\omega) s(\omega, t) + \sqrt{\frac{1}{N}}\zeta_i(t), \quad [6]$$

where Y_0 is the stationary function of y, ζ is a certain stochastic function, and $\mathcal{F}$ is a linear-response function of y against the input $s(\omega, t)$, we can compute the analytical form of Z as

$$Z = \frac{1}{\tau_s^2\sqrt{N}}\left(N\Phi_0^2 + \mathrm{Var}[\zeta] + \mathrm{Var}[\eta] + \tau_s^2 \mathrm{Var}[\dot{\eta}]\right)^{1/2}, \quad [7]$$

where $\Phi_0 = (r_0(b_i) - Y_0(b_i))$ corresponds to the stationary nonspiking behavior. $\dot{\eta}(t)$ is a stochastic process obtained from the derivative of $\eta(t)$ (if $\eta(t)$ is a Gaussian white noise, $\dot{\eta}(t)$ is referred to as purple noise), assuming that the time averages of the stochastic variables $\eta(t)$, $\eta'(t)$, and $\zeta(t)$ are 0. Furthermore, we assumed $s(\omega) = 0$ for simplicity. Eq. **7** indicates that Z is modulated by both N and τ_s.

Configuration of a Musculoskeletal Bipedal Walker. The bipedal body consists of seven rigid bodies: an upper body along with the left and right thighs, shanks, and feet. Each leg of the musculoskeletal system has eight MTUs, resulting in a total of 16 MTUs for the legged system. We used basically the same parameters as ref. 22 except that we use the maximum contract velocity of a muscle $v_{\max}^c = 12 l_{opt}\ \mathrm{s}^{-1}$, where l_{opt} [m] is the optimal muscle length to generate the maximum force. The numerical simulation of the rigid bodies, the joint-limiting dynamics, the body-ground contacts, the ground reaction force, and the MTU forces are integrated by the Open Dynamics Engine (ODE) (68), using a step size of 1 ms.

Base Reflex System. Each leg of a walker has four states: stance, swing initiation, swing, and stance preparation. In each phase, the nonspiking activation signals for the corresponding MTUs are determined using reflex rules proposed in ref. 22. Here, we describe the reflex rules only briefly.

The MTU activation signal is determined by three basic rules: positive force feedback, MTU length feedback, and proportional-derivative (PD) control. The MTU activation R_m^F generated by the positive force feedback rule is determined using the gain G_i^F as $R_i^F = G_i^F F_i^{MTU}(t)$, where $F_i^{MTU}(t)$ is the force generated by the ith MTU. The length feedback rule works to contract the MTU toward the desired length and contributes to MTU activation by R_i^L as $R_i^L = G_i^L [l_i - L_i^g]_+$, where L_i^g is the desired muscle fiber length, and $[z]_+ = z$ if z is positive and 0 otherwise. Likewise, $[z]_- = z$ if z is negative and 0 otherwise. PD control mainly regulates the angle of the upper body and contributes via R_i^θ as $R_i^\theta = K_i^p [\theta(t) - \theta_i^g]_\pm + K_i^d [\dot{\theta}]_\pm$, where θ is the rigid-body posture (such as upper body) or the joint angle (e.g., knee angle), K_i^p is the positional feedback gain, and K_i^d is the derivative feedback gain.

A smooth nonspiking activation signal l_i^r generated by a base reflex system is basically composed of a combination of these three reflex rules as $l_i^r = R_i^F + R_i^L + R_i^\theta + R_i^c - U_i^a$, where R_i^c is the constant activation signal, and U_i^a is inhibitory input from the correspondent antagonist muscle (e.g., TA receives the inhibitory input from its antagonist soleus muscle [SOL] as $U_i^a = F_{SOL}^{MTU}$ during the stance phase).

A smooth, nonspiking activation signal l_i^r (although it is highly nonlinear because of the threshold function $[z]_\pm$) computed by the base reflex system is passed to the corresponding ensemble of N LIF neurons as $I_i(t) = g_i^r l_i^r$, where g_i^r is the input gain. The MTU activation level is determined by the EPSP signal induced by the corresponding neuron ensemble, and the generative force of an MTU is computed based on the dynamics proposed in ref. 23.

A simple reflex controller activates an MTU simply as $A_i(t) = l_i^r(t)$, and a sigmoidal controller activates an MTU using a sigmoid function as $A_i = g_i^s(1/(1 + \exp(-c_i^s l_i^r)) - 1/2)$, where g_i^s is the actuation gain and c_i^s is the input gain.

Optimization of Controllers. The cost function J for the real-coded GA with the BLX-α method (24) was designed so that the center-of-mass (CoM) velocity of the agent was within the range of $v^g \pm 0.1$, where we used the target velocity $v^g = 1.75$ m/s that was correspondent to "very fast walking speed" (22). In particular, we used $J = \frac{1}{T}\int_{t_0}^{t_0+T} J_v\left(|v^g - v\left(t\right)|\right)dt + J_p$, where v^g and v were the desired and actual CoM velocities, respectively, and $J_v\left(z\right) = z$ for $z > 0.1$ m/s and $= 0$ otherwise. We basically used $t_0 = 5$ s and $T = 20$ s but applied $T = 140$ s for 10% individuals to avoid the local minimum. J_p is the penalty term for falling, jumping, toe striking, or stopping (*SI Appendix*, section S2).

A simple reflex controller was obtained by optimizing all parameters of the base reflex systems such as $G_i^{F/L}$, L_i^g, and $K_i^{p/d}$. Please see ref. 22 for the full parameters list of the base reflex system that must be optimized. An sSNN controller was obtained by optimizing all parameters for the base reflex system and the parameters V_i^R, B_i, D_i, g_i^A, and A_i^0 of the sSNN. As for the τ, τ_s, and N, we used the fixed values $\tau = 10$ ms, $\tau_s = 5$ ms, and $N = 40$ during optimization. Likewise, a sigmoidal controller was obtained by optimizing the base reflex systems and the parameters of sigmoid functions g_i^s and c_i^s. Note that the parameters of the base reflex system are different among reflex, sigmoidal, and sSNN controllers. This is because, in general, a reflexive signal that is optimal to drive an MTU via an sSNN or via a sigmoid function is different from the optimal reflexive output required for direct control of an MTU.

ACKNOWLEDGMENTS. This research is based on results obtained from a project commissioned by the New Energy and Industrial Technology Development Organization. Furthermore, this research is partially supported by Japan Society for the Promotion of Science (JSPS) KAKENHI Grant-in-Aid for Early-Career Scientists JP18K18128.

1. A. A. Faisal, L. P. J. Selen, D. M. Wolpert, Noise in the nervous system. *Nat. Rev. Neurosci.* **9**, 292–303 (2008).
2. D. Debanne, A. Bialowas, S. Rama, What are the mechanisms for analogue and digital signalling in the brain?*Nat. Rev. Neurosci.* **14**, 63–69 (2013).
3. W. Maass, To spike or not to spike: That is the question. *Proc. IEEE* **103**, 2219–2224 (2015).
4. Z. Jonke, S. Habenschuss, W. Maass, Solving constraint satisfaction problems with networks of spiking neurons. *Front. Neurosci.* **10**, 118 (2016).
5. L. Leng *et al.*, Spiking neurons with short-term synaptic plasticity form superior generative networks. *Sci. Rep.* **8**, 10651 (2018).
6. B. Lindner, J. García-Ojalvo, A. Neiman, L. Schimansky-Geier, Effects of noise in excitable systems. *Phys. Rep.* **392**, 321–424 (2004).
7. J. Buceta, M. Ibañes, J. M. Sancho, K. Lindenberg, Noise-driven mechanism for pattern formation. *Phys. Rev.* **67**, 021113 (2003).
8. L. S. Tsimring, Noise in biology. *Rep. Prog. Phys.* **77**, 026601 (2014).
9. L. Gammaitoni, P. Hänggi, P. Jung, F. Marchesoni, Stochastic resonance. *Rev. Mod. Phys.* **70**, 223–287 (1998).
10. F. Moss, L. M. Ward, W. G. Sannita, Stochastic resonance and sensory information processing: A tutorial and review of application. *Clin. Neurophysiol.* **115**, 267–281 (2004).
11. K. Matsumoto, I. Tsuda, Noise-induced order. *J. Stat. Phys.* **31**, 87–106 (1983).
12. T. Shinbrot, F. J. Muzzlo, Noise to order *Nature* **410**, 251–258 (2001).
13. P. Joshi, W. Maass, Movement generation with circuits of spiking neurons. *Neural Comput.* **171**, 1715–1738 (2005).
14. N. Brunel, S. Sergi, Firing frequency of leaky integrate-and-fire neurons with synaptic current dynamics. *J. Theor. Biol.* **195**, 87–95 (1998).
15. M. Sreenivasa, K. Ayusawa, Y. Nakamura, Modeling and identification of a realistic spiking neural network and musculoskeletal model of the human arm, and an application to the stretch reflex. *IEEE Trans. Neural Syst. Rehabil. Eng.* **24**, 591–602 (2016).
16. C. Zhou, J. Kurths, Noise-induced phase synchronization and synchronization transitions in chaotic oscillators. *Phys. Rev. Lett.* **88**, 230602 (2002).
17. J. Teramae, D. Tanaka, Robustness of the noise-induced phase synchronization in a general class of limit cycle oscillators. *Phys. Rev. Lett.*, **93**, 204103 (2004).
18. M. Deger, T. Schwalger, R. Naud, W. Gerstner, Fluctuations and information filtering in coupled population of spiking neurons with adaptation. *Phys. Rev.* **90**, 062704 (2014).
19. T. Schwalger, M. Deger, W. Gerstner, Towards a theory of cortical columns: From spiking neurons to interacting neural populations of finite size. *PLoS Comput. Biol.* **13**, e1005507 (2017).
20. D. R. Chialvo, A. Longtin, J. Müller-Gerking, Stochastic resonance in models of neuron ensembles. *Phys. Rev.* **55**, 1798–1808 (1997).
21. S. Yonekura, Y. Kuniyoshi, Y. Kawaguchi, Growth of stochastic resonance in neuronal ensembles with the input signal intensity. *Phys. Rev.* **86**, 011922 (2012). Erratum in: Phys. Rev. E. **93**, 039903 (2016).
22. J. M. Wang, S. R. Hamner, S. L. Delp, V. Koltun, Optimizing locomotion controllers using biologically-based actuators and objectives. *ACM Trans. Graphics* **31**, 1–11 (2012).
23. H. Geyer, H. Herr, A muscle-reflex model that encodes principles of legged mechanics produces human walking dynamics and muscle activities. *IEEE Trans. Neural Syst. Rehabil. Eng.* **18**, 263–273 (2010).
24. L. J. Eshelman, J. D. Schaffer, Real-coded genetic algorithms and interval-schemata. *Found. Genet. Algorithms* **2**, 187–202 (1993).
25. K. J. Nobes *et al.*, A comparison of skating economy on-ice and on the skating treadmill. *Can. J. Appl. Physiol.* **28**, 1–11 (2003).
26. E. A. Hansen, L. A. R. Kristensen, A. M. Nielsen, M. Voigt, P. Madeleine, The role of stride frequency for walk-to-run transition in humans. *Sci. Rep.* **7**, 2010 (2017).
27. K. Mabuchi, K. Tanaka, D. Uchijima, R. Sakai, Frictional coefficient under banana skin. *Tribol. Online* **3**, 147–151 (2012).
28. R. M. Alexander, "Mechanics of bipedal locomotion" in *Perspectives in Experimental Biology*, P. S. Davies, Ed. (Oxford: Pergamon Press, 1976), vol. 1, pp. 493–504.
29. M. H. Dickinson *et al.*, How animals move: An integrative view. *Science* **5463**, 100–106 (2000).
30. I. D. Loram, M. Lakie, Human balancing of an inverted pendulum: Position control by small, ballistic-like, throw and catch movements. *J. Physiol.* **540**, 1111–1124 (2002).
31. M. Casadio, P. G. Morasso, V. Sanguineti, Direct measurement of ankle stiffness during quiet standing: Implication for control modelling and clinical application. *Gait Posture* **21**, 410–424 (2005).
32. J. H. J. Allum, M. G. Carpenter, F. Honegger, A. L. Adkin, B. R. Bloem, Age-dependent variations in the directional sensitivity of balance corrections and compensatory arm movements in man. *J. Physiol.* **542**, 643–663 (2002).
33. C. A. Laughton *et al.*, Aging, muscle activity, and balance control: Physiologic changes associated with balance impairment. *Gait Posture* **18**, 101–108 (2003).
34. C. Assaiante, M. Woollacott, B. Amblard, Development of posture adjustment during gait initiation: Kinematic and EMG analysis. *J. Mot. Behav.* **32**, 211–226 (2000).
35. A. Delafontaine *et al.*, Anticipatory postural adjustments during gait initiation in stroke patients. *Front. Neurol.* **10**, 352 (2019).
36. Y. Kurita, Y. Matsumura, S. Kanda, H. Kinugasa, Gait patterns of quadrupeds and natural vibration modes. *J. Syst. Des. Dyn.* **2**, 1316–1326 (2008).
37. B. D. Robertson, G. S. Sawicki, Unconstrained muscle-tendon workloops indicate resonance tuning as a mechanism for elastic limb behavior during terrestrial locomotion. *Proc. Natl. Acad. Sci. U.S.A.* **112**, E5891–E5898 (2015).
38. T. McGeer, Passive dynamic walking. *Int. J. Robot Res.* **9**, 62–82 (1990).
39. S. M. Pincus, Approximate entropy as a measure of system complexity. *Proc. Natl. Acad. Sci. U.S.A.* **86**, 2297–2301 (1991).
40. C. W. Eurich, J. G. Milton, Noise-induced transitions in human postural sway. *Phys. Rev.* **54**, 6681–6684 (1996).
41. M. Vukobratović, J. Stepanenko, On the stability of anthropomorphic systems. *Math. Biosci.* **15**, 1–37 (1972).
42. H. Machemer, R. Eckert, Electrophysiological control of reversed ciliary beating in paramecium. *J. Gen. Physiol.* **61**, 572–587 (1973).
43. J. A. Wilson, C. E. Phillips, Locust local nonspiking interneurons which tonically drive antagonistic motor neurons: Physiology, morphology, and ultrastructure. *J. Comp. Neurol.* **204**, 21–31 (1982).
44. M. Hiasada, The paraneuronal nature of neurons: Nonspiking communication in the crayfish central nervous system. *Arch. Histol. Cytol.* **52**, 139–146 (1989).
45. M. J. Rodriguez, R. J. Alvarez, L. Szczupak, Effect of a nonspiking neuron on motor patterns of the leech. *J. Neurophysiol.* **107**, 1917–1924 (2012).
46. S. M. Yang, M. E. Vilarchao, L. Rela, L. Szczupak, Wide propagation of graded signals in nonspiking neurons. *J. Neurophysiol.* **109**, 711–720 (2013).
47. M. Davies *et al.*, Loihi: A neuromorphic manycore processor with on-chip learning. *IEEE Micro* **38**, 82–99 (2018).
48. P. A. Merolla *et al.*, A million-neuron integrated circuit with a scalable communication network and interface. *Science* **345**, 668–673 (2016).
49. E. O. Neftci, C. Augustine, S. Paul, G. Detorakis, Event-driven random back-propagation: Enabling neuromorphic deep learning machines. *Front. Neurosci.* **11**, 324 (2017).
50. Y. LeCun, Y. Bengio, G. Hinton, Deep learning. *Nature* **521**, 436–444 (2015).
51. V. Mnih *et al.*, Human-level control through deep reinforcement learning. *Nature* **518**, 529–533 (2015).
52. R. Naud, A. Payeur, A. Longtin, Noise gated by dendrosomatic interactions increases information transmission. *Phys. Rev. X*, **7**, 031045 (2017).
53. M. von Smoluchowski, Experimental nachweisbare, der üblichen thermodynamik widersprechende molekularphänomene. *Phys. Zeitchrift* **13**, 1069–1080 (1912).
54. R. P. Feynman, R. B. Leighton, M. Sands, *The Feynman Lectures on Physics* (Addison-Wesley, 1963), chap. 46.
55. G. Karpati, *Disorders of Voluntary Muscle* (Cambridge University Press, ed. 8, 2010).
56. B. P. Bean, The action potential in mammalian central neurons. *Nat. Rev. Neurosci.* **8**, 451–465 (2007).
57. B. Hochner, M. Klein, S. Schacher, E. R. Kandel, Action-potential duration and the modulation of transmitter release from the sensory neurons of *Aplysia* in presynaptic facilitation and behavioral sensitization. *Proc. Natl. Acad. Sci. U.S.A.* **83**, 8410–8414 (1986).
58. A. O. Verkerk, G. S. C. Geuzebroek, M. W. Veldkamp, R. Wilders, Effects of acetylcholine and noradrenalin on action potentials of isolated rabbit sinoatrial and atrial myocytes. *Front. Physiol.* **3**, 174 (2012).
59. M. R. Carey, W. G. Regehr, Noradrenergic control of associative synaptic plasticity by selective modulation of instructive signals. *Neuron* **62**, 112–122 (2008).

60. M. E. Hasselmo, B. P. Fehlau, Differences in time course of ACh and GABA modulation of excitatory synaptic potentials in slices of rat hippocampus. *J. Neurophysiol.* **86**, 1792–1802 (2001).
61. K. Nozaki, R. Kubo, Y. Furukawa, Serotonin modulates the excitatory synaptic transmission in the dentate granule cells. *J. Neurophysiol.* **115**, 2997–3007 (2016).
62. S. Errchidi, G. Hilaire, B. Monteau, Permanent release of noradrenaline modulates respiratory frequency in the newborn rat: An in vitro study. *J. Physiol.* **429**, 497–510 (1990).
63. A. M. Cabaj *et al.*, Serotonin controls initiation of locomotion and afferent modulation of coordination via 5-HT_7 receptors in adult rats. *J. Physiol.* **595**, 301–320 (2016).
64. I. A. Rybak, J. F. Paton, J. S. Schwaber, Modeling neural mechanisms for genesis of respiratory rhythm and pattern. I. Models of respiratory neurons. *J. Neurophysiol.* **77**, 1994–2006 (1997).
65. N. A. Shevtsova *et al.*, Organization of left-right coordination of neuronal activity in the mammalian spinal cord: Insights from computational modelling. *J. Physiol.* **593**, 2403–2426 (2015).
66. H. E. Plesser, T. Geisel, Markov analysis of stochastic resonance in a periodically driven integrate-and-fire neuron. *Phys. Rev.* **59**, 7008–7017 (1999).
67. A. Destexhe, M. Rudolph, J.-M. Fellous, T. J. Sejnowski, Fluctuating synaptic conductances recreate *in vivo*-like activity in neocortical neurons. *Neuroscience* **9**, 13–24 (2001).
68. R. Smith, Open dynamics engine. http://ode.org. Accessed 27 April 2019.